

Structural Dynamics of Ultrathin Cobalt Oxide Nanoislands under Potential Control

Corinna Stumm, Manon Bertram, Maximilian Kastenmeier, Florian D. Speck, Zhaozong Sun, Jonathan Rodríguez-Fernández, Jeppe V. Lauritsen, Karl J. J. Mayrhofer, Serhiy Cherevko, Olaf Brummel,* and Jörg Libuda

Cobalt oxide is a promising earth abundant electrocatalyst and one of the most intensively studied oxides in electrocatalysis. In this study, the structural dynamics of well-defined cobalt oxide nanoislands (NIs) on Au(111) are investigated in situ under potential control. The samples are prepared in ultra-high vacuum and the system is characterized using scanning tunneling microscopy (STM). After transfer into the electrochemical environment, the structure, mobility, and dissolution is studied via in situ electrochemical (EC) STM, cyclic voltammetry, and EC on-line inductively coupled plasma mass spectrometry. Cobalt oxide on Au(111) forms bilayer (BL) and double-bilayer NIs (DL), which are stable at the open circuit potential ($0.8 V_{\text{RHE}}$). In the cathodic scan, the cobalt oxide BL islands become mobile at potentials of $0.5 V_{\text{RHE}}$ and start dissolving at potentials below. In sharp contrast to the BL islands, the DL islands retain their morphology up to much lower potential. The re-deposition of Co aggregates is observed close to the reduction potential of Co^{2+} to Co^{3+} . In the anodic scan, both the BL and DL islands retain their morphology up to $1.5 V_{\text{RHE}}$. Even under these conditions, the islands do not show dissolution during the oxygen evolution reaction (OER) while maintaining their high OER activity.

1. Introduction

Electrochemical water splitting is one of the key technologies for renewable energy storage.^[1] For a broad implementation of water splitting, efficient and stable electrocatalysts are essential. While electrocatalysts for the hydrogen evolution reaction (HER) based on Pt-group metals and achieve high efficiency,^[2] the development of catalysts for the oxygen evolution reaction (OER) is much more challenging. Only few materials show significant activity for this reaction. The majority of the OER active catalysts in acidic media are made of rare and expensive noble metal oxides namely IrO_2 and RuO_2 .^[3] It was demonstrated that also oxides made from earth abundant 3d metals such as Ni, Fe, and in particular Co show promising results in alkaline media.^[2,4] For example, cobalt oxide is highly active over a broad range of pH values from near neutral to alkaline

conditions.^[5] However, the chemical and structural behavior is complex and involves several potential- and pH-dependent transformations.^[4c,6] Starting from initially inactive phases (Co_3O_4 , CoO), layered $\text{CoO}(\text{OH})$ oxyhydroxides, and $\text{Co}(\text{OH})_2$ hydroxides are formed during OER.^[5a,7] Recent studies suggest that the active centers for OER are Co^{4+} species^[6c,8] and that their activity is related to $\text{CoO}(\text{OH})$ oxyhydroxide-like structures.^[9] While the exact nature of the active site is still under debate,^[10] it is clear that there is a lot of potential to further improve the catalytic properties. Both the overpotential for OER and the stability depend, for example, on nanostructuring,^[11] doping,^[2,12] and synergistic effects, for example, with noble metals.^[8,13] In specific, it has been shown that cobalt oxide on gold shows improved catalytic performance, poisoning resistance, and stability.^[14]

In order to understand such effects at the atomic scale, it is essential to explore the structural properties of well-defined cobalt oxide nanostructures under reaction conditions.^[15] In this work, we present the results of a model catalytic study on ultraclean and well-defined cobalt oxide model electrocatalysts prepared by surface science methods in ultra-high vacuum (UHV).^[16] The cobalt oxide nanoislands (NIs) grown on Au(111) were previously characterized in great detail by scanning tunneling microscopy (STM), X-ray photoelectron spectroscopy (XPS) and density-functional theory calculations.^[17] In particular it was shown that the promotional effect of Au


C. Stumm, Dr. M. Bertram, M. Kastenmeier, Dr. O. Brummel, Prof. J. Libuda
Interface Research and Catalysis
ECRC

Friedrich-Alexander-Universität Erlangen-Nürnberg
Egerlandstraße 3, 91058 Erlangen, Germany
E-mail: olaf.brummel@fau.de

Dr. F. D. Speck, Prof. K. J. J. Mayrhofer, Dr. S. Cherevko
Helmholtz Institute Erlangen-Nürnberg for Renewable Energy (IEK-11)
Forschungszentrum Jülich GmbH
Egerlandstraße 3, 91058 Erlangen, Germany

Dr. Z. Sun, Dr. J. Rodríguez-Fernández, Prof. J. V. Lauritsen
Interdisciplinary Nanoscience Centre (iNANO)
Aarhus University
Gustav Wieds Vej 14, Aarhus C, Aarhus 8000, Denmark

Dr. J. Rodríguez-Fernández
Department of Physics
University of Oviedo
Oviedo, Spain

 The ORCID identification number(s) for the author(s) of this article can be found under <https://doi.org/10.1002/adfm.202009923>.

© 2021 The Authors. Advanced Functional Materials published by Wiley-VCH GmbH. This is an open access article under the terms of the Creative Commons Attribution License, which permits use, distribution and reproduction in any medium, provided the original work is properly cited.

DOI: 10.1002/adfm.202009923

as a substrate originates from the stabilization of highly active oxygen at the Co/Au interface.^[17a]

After preparation, the atomically defined model catalysts were transferred into the electrochemical environment while preserving their surface structure.^[16a,b] In previous electrochemical (EC) ex situ studies using UHV STM some of the authors demonstrated that the gold substrate may stabilize 2D islands and suppress the formation of less active bulk oxide.^[17d] It was speculated that the gold stabilizes active CoO(OH)-like phases in a wide potential range and, thus, lowers the potential at which the active phase is formed.^[17d] However, in situ studies are necessary to verify this hypothesis under operation conditions.

We address this essential question by EC-STM.^[18] EC-STM is particularly well suited to study ultrathin islands on metallic supports and is capable of providing structural information with highest resolution directly under potential control. However, the method is highly demanding from the experimental side and only few oxide surfaces have been investigated so far, for example, rutile TiO₂^[19] and FeO/Pt(111).^[20] Few EC-STM studies

have been performed on single crystalline Co electrodes,^[21,22] however, there is no such study on a layered cobalt oxide to date. Here, we present the first in situ EC-STM study on this important class of materials, focusing on the particularly promising case of cobalt oxide NIs on Au(111). In addition, we combine the EC-STM studies with cyclic voltammetry (CV) and on-line inductively coupled plasma mass spectrometry (ICP-MS) to correlate the structure properties of the NIs with their activity and dissolution behavior.

2. Results and Discussion

2.1. General Appearance in UHV, Air, and Electrolyte

In a first step, we investigated the appearance of the UHV-prepared cobalt oxide NIs in UHV and in the electrolyte. In **Figure 1a**, we show the clean Au(111) surface in UHV with its characteristic herringbone reconstruction.^[23] After deposition,

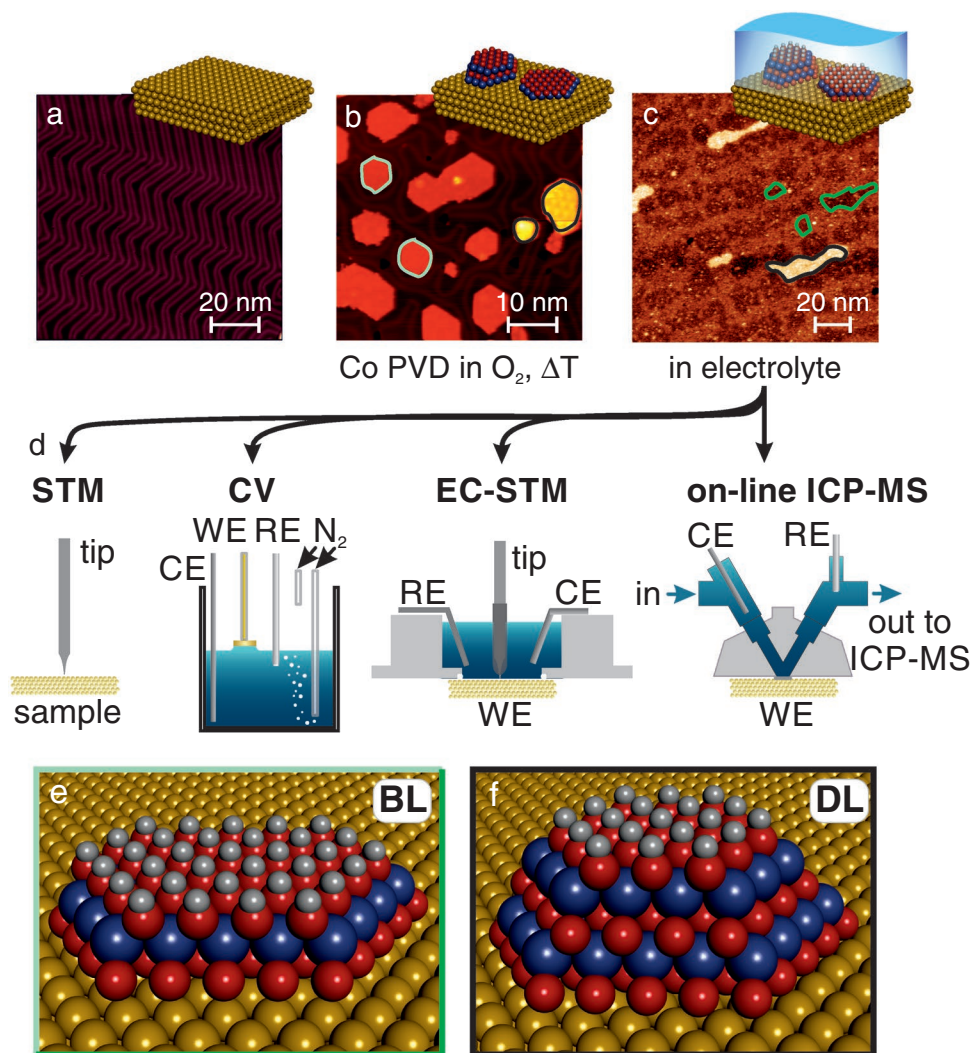


Figure 1. STM images of a) a clean Au(111) surface in UHV, b) CoO_x NIs in UHV, and c) in 0.1 m phosphate buffer at pH 10 (0.7 V_{RHE}); STM images were measured with a) -1.25 V/-0.35 nA; b) -1.25 V/-0.24 nA c) 0.3 V/0.20 nA; d) schematic representation of the methods used in this study: STM, CV, EC-STM, and EC on-line ICP-MS/SFC; Schematic representation of the CoO_x e) bilayer and f) double-bilayer in liquid environment.

the CoO_x NIs appear as flat, island-like features with a predominantly hexagonal shape with two distinct apparent heights. The apparent height of the major lower islands is $1.7 \pm 0.2 \text{ \AA}$ relative to the underlying Au(111) surface and shows a moiré pattern with a periodicity of $37 \pm 2 \text{ \AA}$ (see Figure 1b, marked in light green). The higher islands have an apparent height of $4.0 \pm 0.2 \text{ \AA}$ and a moiré pattern with a periodicity of $31 \pm 2 \text{ \AA}$ (marked in black). Comparing these values with previous studies, we conclude that the NIs grow in form of lower bilayers (BL) and higher double bilayers (DL).^[17a] The Au(111) surface reconstruction is slightly disturbed at the locations of the CoO_x NIs.

When the sample is imaged with EC-STM in the electrolyte (Figure 1c), the unreconstructed Au(111) surface is covered by two types of islands with different apparent heights. The major species are smaller depressions (inverse islands) with an apparent depth of 1.0 \AA ($\pm 0.1 \text{ \AA}$) (marked in dark green). Additionally, larger islands are present (marked in black), which exhibit an irregular shape and have an apparent height of 3.1 \AA ($\pm 0.3 \text{ \AA}$) with respect to the Au(111) surface. Both island types show no moiré pattern. Also, the STM image appears noisier and several small bright dots are visible. We attribute this effect to phosphate species adsorbing from the electrolyte.

The CoO_x BL and DL islands experience structural changes upon immersion in electrolyte (see Figure 1e). In previous experiments, we investigated the state of the $\text{CoO}_x/\text{Au}(111)$ system prior to and after immersion in ultrapure water and 0.1 M NaOH .^[17d] We found that the BL NIs are still observable by UHV-STM on the surface after immersion in both liquid environments. We noticed that the NIs structure changes during transfer from UHV to ambient conditions and exposure to electrolyte. An additional O layer is intercalated and a trilayer structure is formed.^[17f] Based on these results and the UHV images presented in this paper, we assign the inverse islands observed in electrolyte to the BL species and the larger island type to the DL NI structure, both with an additional intercalated O-layer. To simplify the labeling, we still use the terms BL and DL in the following discussion to emphasize the correlation between the UHV-prepared and ambient-condition structures.

The overall coverage of the cobalt oxide NI as determined from several STM images (see Figure S1, Supporting Information) was 39% ($\pm 6\%$) in average. Note that this value is higher than the coverage of 30% as determined for the sample imaged in UHV.

The observed difference in apparent height of both of the NIs types in electrolyte and UHV can have different origins. First, an apparent height change of the islands arises from the different tunneling barriers in UHV and electrolyte (as a result of adsorption of H_2O and other molecules from the electrolyte or the gas phase). Most importantly, however, the tunneling bias (U_b) also influences the apparent height of oxides. We studied this effect in more detail by imaging the same location with different bias voltages (see Figure 2, for simplicity, these experiments were performed in air). Again, the Au(111) surface (marked in yellow) was covered by BL (green) and DL (black) NIs. The height distribution at different tunneling biases is displayed in Figure 2d. We observe that the apparent height of 3.1 \AA of the DL NIs with respect to the Au(111) surface is independent of the tunneling bias. In sharp contrast, the BL NIs appear as depressions (marked in dark green) at $U_b = 0.4 \text{ V}$ (see Figure 2a) with an apparent depth of 1.0 \AA ($\pm 0.1 \text{ \AA}$). When increasing the bias (see Figure 2b,c), these depressions turn

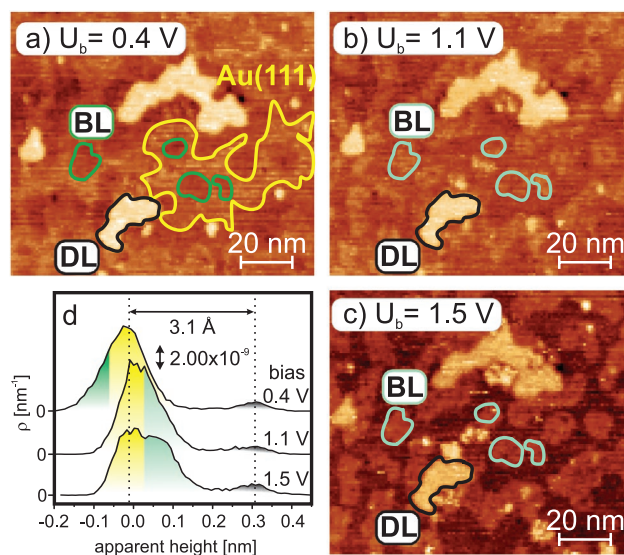


Figure 2. STM images of CoO_x NIs on Au(111) measured at the same spot with varying tunneling bias voltages of a) 0.4 V , b) 1.1 V , and c) 1.5 V . These STM images were measured in air using a tunneling current of 0.2 nA . Different features are identified, which are assigned to Au(111) (yellow), bilayers (BL, blue) and double-bilayers (DL, black). The apparent height of the bilayer is dependent on the tunneling bias voltage and negative and positive apparent heights of the bilayer are illustrated in dark and light green, respectively. d) Comparison of the height distributions dependent on the tunneling bias voltages.

into protrusions (marked in light green) reaching an apparent height of 1.0 \AA ($\pm 0.1 \text{ \AA}$) at $U_b = 1.5 \text{ V}$. We provide additional data on the appearance at negative bias voltages in the Supporting Information (Figure S2, Supporting Information).

Such a behavior is well known for oxides.^[24] If the bias voltage lies inside the bandgap of the oxide film, the islands appear as depressions, as the tunneling occurs through the oxide. At higher energies, the oxides appear as bright protrusions, as the bias voltage lies outside of the bandgap. A more detailed explanation of the tunneling mechanism is given in Chapter 3, Supporting Information. This behavior was observed, for example, for CoO islands on Ag(100)^[25] and Pt(111),^[26] for a thin CoO layer on Fe(001),^[27] and for NiO on Ag(100).^[24] In contrast to the BL, the apparent height of the DL features is independent of the bias voltage. In the DL, cobalt is present in the oxidation states Co^{2+} and Co^{3+} , assuming a hydroxylated surface at ambient conditions, while in the BL, it is only present as Co^{3+} .^[17f] This difference in oxidation states leads to a change in the band structure. Specifically, the band gap of spinel type cobalt oxide, which also comprises Co^{2+} and Co^{3+} , is narrow as compared to the rock-salt structure (comprising Co^{2+} only).^[28] As a consequence, the bias voltage applied in our experiments always lies outside of the band gap for the DL islands and inside of the band gap for the BL islands. This explains the difference in the bias voltage dependence between the DL and BL islands.

2.2. Electrochemical Characterization

In a next step, we characterized the cobalt oxide NIs electrochemically by CV in hanging meniscus configuration. In

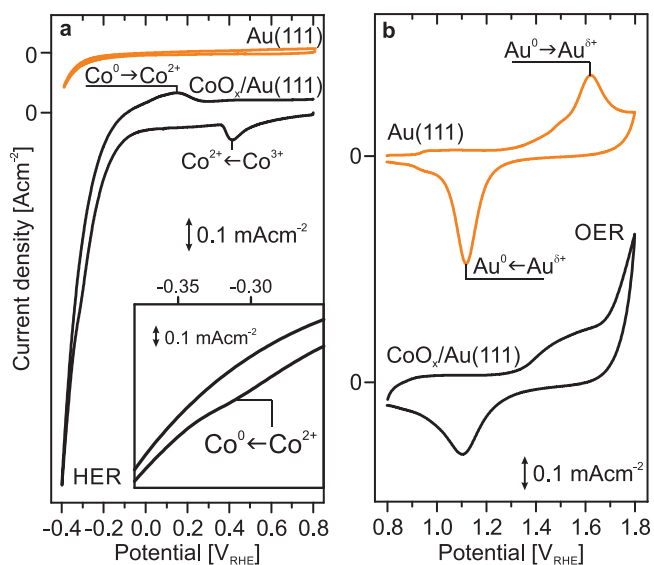


Figure 3. Comparison of the cyclic voltammograms of the bare Au(111) electrode (orange) and the cobalt oxide NIs supported on Au(111) (black) at potentials a) below and b) above the OCP of 0.8 V_{RHE} . The inset in a) depicts the potential region around $-0.3 V_{\text{RHE}}$ with different scaling. The CVs were recorded with a scan rate of $0.05 V s^{-1}$ in 0.1 M phosphate buffer at pH 10.

a previous study, we demonstrated that cobalt oxide shows highest structural stability at pH 10.^[29] Therefore, we used 0.1 M phosphate buffer at pH 10 as an electrolyte. The samples were immersed under potential control at the open circuit potential (OCP) of 0.8 V_{RHE} . We measured CVs between 0.8 and $-0.4 V_{\text{RHE}}$ (Figure 3a, black curves) and 0.8 and 1.8 V_{RHE} (Figure 3b, black curves) at a scan rate of $0.05 V s^{-1}$. The samples were freshly prepared for each experiment. For comparison, we also recorded CVs of Au(111) (Figure 3, orange) under identical conditions. Figure 3 shows the first cycle of each experiment, while we provide the full set of the 10 subsequent potential cycles in Figure S3, Supporting Information. A single feature is observed in the cathodic scan direction on the bare Au(111) electrode (orange curve) below $-0.2 V_{\text{RHE}}$, which we assign to the HER. However, the current densities are relatively low and reach $0.13 mA cm^{-2}$ at $-0.4 V_{\text{RHE}}$. In contrast, the CV of the surface covered with NIs shows multiple features. In negative scan direction, we observe a peak at $0.40 V_{\text{RHE}}$, which we assign to the reduction of Co^{3+} to Co^{2+} . Note that cobalt is mostly present in valence state Co^{3+} after exposure to air.^[17f] At $-0.05 V_{\text{RHE}}$ we observe the onset of a negative current, which we assign to the HER.^[17d] Superimposed on the HER, there is an additional shoulder at $-0.30 V_{\text{RHE}}$ (see inset in Figure 3a), which we attribute to the reduction of Co^{2+} to Co^0 (compare, e.g., the Pourbaix diagram in Ref. [30]). In the reverse sweep, there is a single feature at $0.3 V_{\text{RHE}}$, which we consequently attribute to the reoxidation of Co^0 to Co^{2+} . No further peaks are observed below 0.8 V_{RHE} , suggesting that cobalt oxide remains in the oxidation state 2+ after cycling (see also the Pourbaix diagram in Ref. [6a]).

Apparently, the NI covered surface exhibits much higher activity in the HER (current density of $1.1 mA cm^{-2}$ at $-0.4 V_{\text{RHE}}$) compared to the bare Au(111) electrode. We did not

observe a feature associated with the reduction of Co^{3+} to a mixed Co^{2+}/Co^{3+} state, as expected for the transition of $CoOOH$ to Co_3O_4 .^[29] In a previous study, some of the authors employed XPS to show that indeed the valence state transitions between layered cobalt oxide $CoO_{2-x}(OH)_x$ NI phases on Au(111) occur directly without passing through the structurally very different spinel-type Co_3O_4 phase.^[17d]

The CVs probing the positive potential limit are dominated by features which we ascribe to the oxidation and reduction of the Au(111) surface.^[31] In the anodic scan, the features assigned to Au oxidation appear between 1.35 and 1.65 V_{RHE} with a maximum at 1.6 V_{RHE} . In the reverse scan, the gold oxide is reduced to the metallic state at 1.1 V_{RHE} . In the presence of the cobalt oxide NIs, the gold redox features are weaker due to partial blocking of the surface. In literature it is reported that cobalt oxide is oxidized from Co^{3+} to Co^{4+} at potentials around 1.45–1.55 V_{RHE} forming CoO_2 .^[32] We cannot exclude such a process, which would overlap with the broad Au features. Above 1.7 V_{RHE} , the current density increases steeply and reaches $0.4 mA cm^{-2}$ at 1.8 V_{RHE} . We assign this feature to OER, indicating that the CoO_x NIs are highly active for OER, while plane Au(111) is inactive. Noteworthy, the use of atomically defined model surfaces also enables us to calculate the precise turnover frequencies (TOF). Details are described in the Supporting Information. For the CoO_x NIs, the TOF is 1.1 electrons per cobalt atom per second at 1.8 V_{RHE} , assuming that all Co atoms participate at equal basis.

2.3. Structural Dynamics and Dissolution at Potentials Below OCP

In order to correlate morphology and activity of the NIs, we investigated the changes of the surface structure upon reduction by EC-STM. The experiment was performed using a coated W tip in 0.1 M phosphate buffer at pH 10. In Figure 4a, we depict the measurement procedure schematically. First, the surface was scanned at 0.7 V_{RHE} . Then, the potential was decreased stepwise from 0.7 to 0.2 V_{RHE} . During all measurements, the potential of the W tip was held constant at 0.4 V_{RHE} . At each potential step, two subsequent images were recorded at identical locations. The time delay between the two subsequent images was 3 min at 0.7 V_{RHE} and 15 min for all other potentials.

At 0.7 V_{RHE} no morphological changes are observed after 3 min (Figure 4b). In an additional experiment, we recorded images at this potential at different locations over a total period of 42 min (see Figure S4, Supporting Information). Also in these data, we could not identify any changes of the NI morphology. These findings suggest that the NIs are stable over a long period of time at 0.7 V_{RHE} . After stepping to 0.5 V_{RHE} , the apparent height of the BL islands changes from depressions to protrusions. Simultaneously, the BL islands become mobile on the surface. Selected areas where this mobility is particularly apparent are highlighted by a white circle in Figure 4. Additionally, we provide a video composed of several images at 0.5 and 0.4 V_{RHE} as supporting material. These videos illustrate the type of mobility more clearly and show that the islands change their shape dynamically with time. The mobility of the BL islands is accompanied by continuous dissolution of the CoO_x

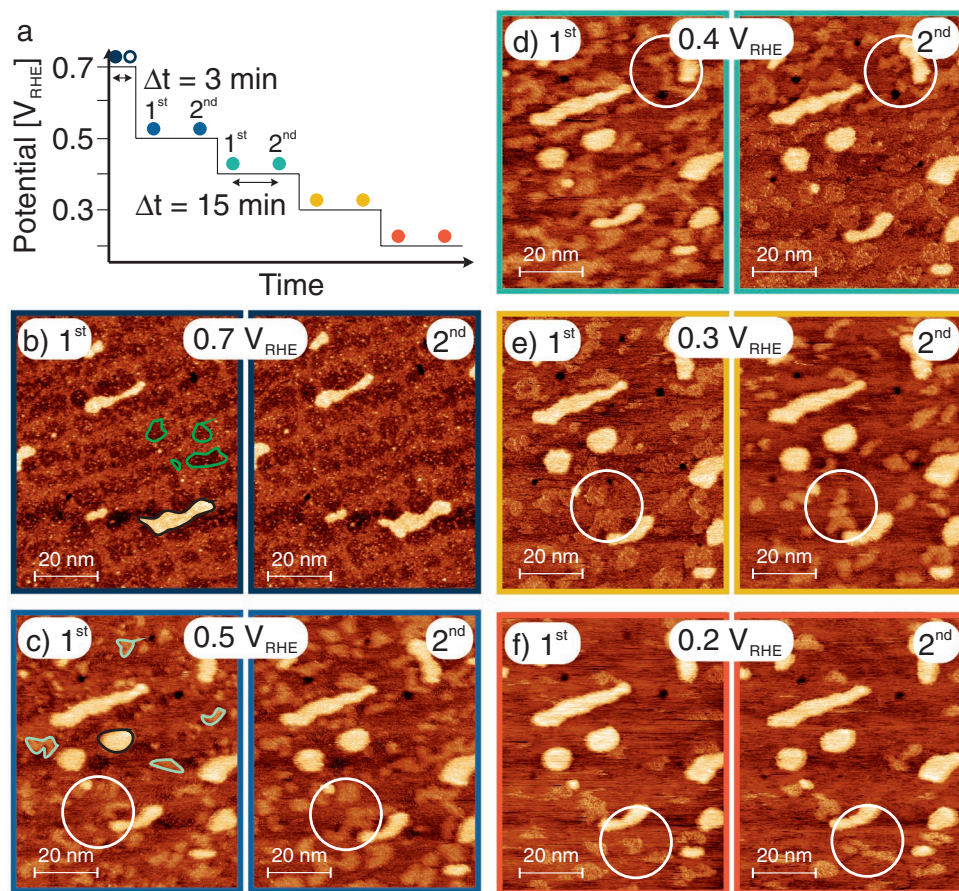


Figure 4. EC-STM images of cobalt oxide NIs on Au(111) between 0.7 and 0.2 V_{RHE} . Two images are shown at the same imaging position with a time difference of 3 min (0.7 V_{RHE}) and 15 min (all other potentials). Major differences between the first and second image at the same potential are marked by white circles. The potential applied to the W-tip was kept constant at 0.4 V_{RHE} and the tunneling current was 0.6 nA.

NIs. The dissolution becomes very pronounced upon stepping to 0.2 V_{RHE} . Here, only a small fraction of the initial BL structures remains present on the Au surface. It is noteworthy that in sharp contrast to the BL islands, the DL islands do not show any indication for dissolution or mobility under identical conditions.

At 0.8 V_{RHE} , cobalt in the BL islands is present as Co^{3+} and in the DL islands as a mixture of Co^{3+} and Co^{2+} .^[17f] When lowering the potential, Co^{3+} is reduced to Co^{2+} at 0.5 V_{RHE} , as already shown in the CV in Figure 3a. Reduction of the oxide will also change its electronic band structure. It is likely that the change in apparent height of the BL islands upon reduction is due to narrowing of the band gap, which enables tunneling directly into states of the CoO_x NIs. In fact, it is unlikely that the change in contrast in this experiment originates from a change of the tunneling bias as observed in air. The corresponding bias voltages do not agree with the bias voltages applied in this experiment.

We conclude that the reduced BL islands are less stable than the oxidized ones, as indicated by their mobility on the surface. We suggest that the mobility of the islands is caused by fast dissolution and redeposition processes. Surprisingly, the DL islands are fully stable under identical conditions. We attribute this difference to a stabilizing effect of the underlying oxide

layer on the top layer. Similar effects were already observed for platinum oxide on cobalt oxide.^[16a] We also expect less structural rearrangement in the DL features, as only a fraction of the cobalt ions changes its oxidation state.

Next, we investigated the surface morphology in the potential region of hydrogen evolution with a freshly prepared sample. **Figure 5a** shows the potentials at which the following EC-STM images were recorded. In these experiments, a coated PtIr tip was used instead of the W tip to prevent undesirable deposition of WO_x .^[19b] The tip was held at a potential of 0.5 V_{RHE} . The STM scan was started immediately after applying the respective potential and the scan direction is from the top to the bottom. The acquisition time per EC-STM image was 4.3 min. With this information in mind, we note that the STM images also contain some time-dependent information along the scanning direction (note that in Figure 5e,f only the first 3.7 min are shown as the lower part of the image was perturbed). The insets show details of selected flat areas on the surface. At 0.1 V_{RHE} (Figure 5b), the morphology of the surface resembles the situation at 0.2 V_{RHE} in Figure 4. However, a larger amount of BL NIs is still present on the surface, as the surface was kept at low potentials for a shorter time as compared to the experiment shown in Figure 4. In addition, we identify double-row features (see inset) on the underlying Au(111) support, which are typical for the Au(111)

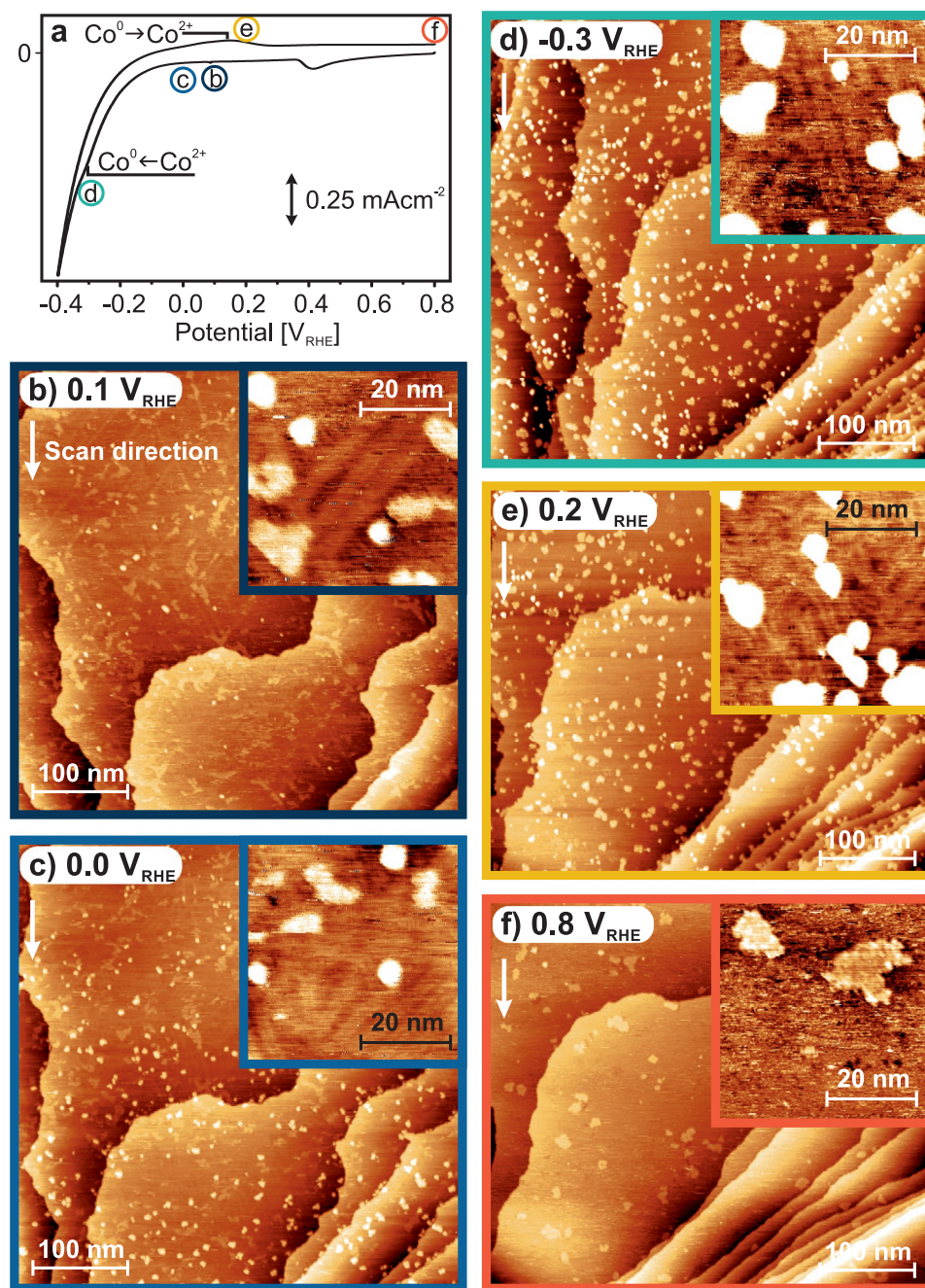


Figure 5. EC-STM images of cobalt oxide NIs supported on Au(111) in the cathodic scan between 0.1 and $-0.3 V_{\text{RHE}}$ and in the anodic scan between -0.4 and $0.8 V_{\text{RHE}}$. a) CV of the sample showing the potentials at which the EC-STM images are measured; EC-STM images measured in the cathodic scan at b) $0.1 V_{\text{RHE}}$, c) $0.0 V_{\text{RHE}}$, and d) $-0.3 V_{\text{RHE}}$ and in the anodic scan at e) $0.2 V_{\text{RHE}}$ and f) $0.8 V_{\text{RHE}}$. The respective potential was applied before the imaging scan was started from the bottom. The potential applied to the PtIr-tip was kept constant at $0.5 V_{\text{RHE}}$ and the tunneling current was 0.8 nA .

herringbone reconstruction (see also Figure 1a).^[23] Schlaup and Horch demonstrated that adsorption of phosphate on Au(111) lifts the herringbone reconstruction.^[33] Therefore, the appearance of the herringbone reconstruction indicates that the phosphate desorbs from the Au(111) terraces in this potential range.

After the potential step to $0.0 V_{\text{RHE}}$ (Figure 5c), small aggregates form with an apparent height of 3.0 \AA ($\pm 0.3 \text{ \AA}$). This height is in agreement with the apparent height of the DL NIs

and, consequently, we attribute the features to this species. The transformation of BL to DL islands occurs gradually during the scan over a period of 2 min after the potential step. Thereafter no further changes of the surface morphology are observed.

At $-0.3 V_{\text{RHE}}$ (Figure 5d), an additional type of islands forms with an apparent height of 5.6 \AA ($\pm 0.5 \text{ \AA}$). These islands appear directly after the potential step and no time-dependent development can be resolved by STM. The height of this feature

agrees with the expected height for 3 monolayers (ML) of metallic cobalt.^[34] Indeed, it is known from literature that Co prefers to adsorb on Au(111) in form of 3D multilayer structures rather than in form of MLs.^[35] Moreover, the potential value of $-0.3 V_{\text{RHE}}$ is in perfect agreement with the reduction peak which we observed in the CV (Figure 3). Therefore, we assigned these features to the deposition of metallic cobalt. In addition, the close-up in Figure 5d shows that the major part of the Au(111) surface has reconstructed under these conditions. EC-STM images in the reverse sweep were recorded at $0.2 V_{\text{RHE}}$ (Figure 5e) and $0.8 V_{\text{RHE}}$ (Figure 5f). We observe that both the metallic cobalt islands and the DL islands dissolve. Only few islands reside on the surface mostly with the apparent height of the BL NIs.

Our observations show that the cobalt oxide NIs become highly dynamic at the onset of reduction of Co^{3+} to Co^{2+} and below. Reduction is accompanied by restructuring, dissolution, and redeposition processes which strongly depend on the initial structure and composition of the NIs. In the next step, we correlate the restructuring processes shown by EC-STM with dissolution as recorded by on-line ICP-MS/scanning flow cell (SFC) experiments. The SFC was connected to the freshly prepared sample at $0.8 V_{\text{RHE}}$ and kept at this potential for 200 s. To obtain potential-resolved information, we recorded two CVs with a scan rate of 2 mV s^{-1} between 0.8 and $-0.4 V_{\text{RHE}}$ (Figure 6a). In an additional experiment, the potential was directly stepped from $0.8 V_{\text{RHE}}$ to selected potentials between 0.5 and $0.0 V_{\text{RHE}}$ (Figure 6b) to obtain time-resolved information. For both experiments, we monitored the dissolution signals of ^{59}Co and ^{197}Au by ICP-MS. Each experiment was performed on a fresh area of the sample.

In Figure 6a the first cathodic scan (black trace) shows no potential dependent Co dissolution in the potential sweep experiment down to $0.6 V_{\text{RHE}}$. Note that the background signal (around $0.06 \text{ ng cm}^{-2} \text{ s}^{-1}$) results from the natural abundance of tiny traces of Co which are present even in Suprapur electrolytes. The naturally less abundant Au is found with much lower probability. At $0.5 V_{\text{RHE}}$, the Co dissolution signal starts to rise and reaches a maximum of $0.11 \text{ ng cm}^{-2} \text{ s}^{-1}$ at $0.3 V_{\text{RHE}}$. Afterward the dissolution rate decreases again and finally returns to its original value. Substantial dissolution of Co is observed in the reverse sweep (red trace) starting from $0.0 V_{\text{RHE}}$ and continuing up to the initial potential value of $0.8 V_{\text{RHE}}$. In the second cycle, the peak at $0.5 V_{\text{RHE}}$ is suppressed in the cathodic scan, while in the anodic sweep the dissolution is comparable to the first cycle. No Au dissolution is detected during potential cycling to negative potentials.

We correlate the ICP-MS data with observations by EC-STM and CV as discussed above. Apparently, the dissolution at $0.5 V_{\text{RHE}}$ results from reduction of Co^{3+} to Co^{2+} . The dissolution rate decreases at lower potentials, where the redeposition of additional DL islands was observed by EC-STM. No additional dissolution is observed upon the reduction of Co^{2+} to Co^0 at $-0.3 V_{\text{RHE}}$. However, reoxidation of Co^0 to Co^{2+} triggers the dissolution of a substantial amount of Co species. As no Co^{3+} is formed after the first cycle, we also do not expect any dissolution feature at $0.5 V_{\text{RHE}}$ in the second cycle, in accordance with the experimental observations. Nevertheless, there is still cobalt oxide present on the surface, which undergoes reduction to Co^0 and subsequent dissolution upon reoxidation to Co^{2+} .

The corresponding potential step experiments are shown in Figure 6b. For the potential step from 0.8 to $0.5 V_{\text{RHE}}$, we observe a transient dissolution process with an exponential decay time of $t_{1/2} = 113 \text{ s}$. Quantitative analysis shows that the fraction of dissolved Co is equivalent to $91\% \pm 15\%$ and $35\% \pm 15\%$ of the initially deposited cobalt for step experiments to 0.5 and $0.4 V_{\text{RHE}}$, respectively (details of the quantitative analysis are given in the Supporting Information). It has to be noted that the dissolution signals at 0.3 and $0.2 V_{\text{RHE}}$ only marginally exceed the detection limit of Co in the on-line ICP-MS ($0.008 \text{ ng cm}^{-2} \text{ s}^{-1}$) and, consequently, cannot be evaluated quantitatively. Noteworthy, for the step experiment to $0.0 V_{\text{RHE}}$ the dissolution rate is below the detection limit. We suggest that the reason for the pronounced potential dependence is the redeposition process observed in EC-STM. After the potential step, dissolution and redeposition compete, while the precipitation rate increases with decreasing potential. The mobility observed for the BL NIs below the Co^{3+} reduction potentials supports this hypothesis.

2.4. Structural Dynamics and Dissolution at Potentials Above OCP

Cobalt oxide is an excellent electrocatalyst for OER.^[5] Therefore we investigated the structural properties of the model catalyst in a potential region from OCP to the OER region by EC-STM. The potentials at which EC-STM images were measured are indicated in the CVs shown in Figure 7a. For all EC-STM experiments, we used coated W tips held at a constant potential of $0.35 V_{\text{RHE}}$.

In Figure 7b–d we compare EC-STM images recorded at 0.8 , 1.0 , and $1.1 V_{\text{RHE}}$, respectively. Very clearly, we observe a change of contrast of the BL islands. At $1.1 V_{\text{RHE}}$, we observe the appearance of striped features oriented in hexagonal symmetry on top of the DL NIs (marked in blue in the inset). The features show an apparent height of 3.1 \AA relative to the Au(111) surface, as is seen in the height distribution shown in Figure 7e. At $1.2 V_{\text{RHE}}$ (Figure 7f), the apparent height of all DL islands changes to 3.1 \AA , a value which is identical to those of the before mentioned stripes. At $1.5 V_{\text{RHE}}$ (Figure 7g) round features appeared which are distributed over the whole surface. At even higher potential, we could not achieve stable imaging conditions anymore. To obtain some information on the structural transformations at even higher potential, we kept the sample at $1.8 V_{\text{RHE}}$ for 20 min, switched back to $0.8 V_{\text{RHE}}$ and measured an additional image (Figure 7h). As compared to the image recorded at the same potential prior to the potential change, we observed additional small islands with an apparent width of 2 to 5 nm and an apparent height of 2.4 \AA ($\pm 0.2 \text{ \AA}$). In addition, the DL islands were found to agglomerate into larger islands.

The change of contrast occurring between 0.8 and $1.1 V_{\text{RHE}}$ results from the change of the tunneling bias, as the tip is held at constant potential during the whole experiment. The change of contrast is observed at similar bias voltages as in the corresponding experiment in air (see Figure 2). The oriented stripes on the BL NIs resemble features, which were observed previously on cobalt- and iron oxide islands by STM in UHV when increasing the oxygen pressure during preparation.^[17a,36] The lines were identified as rows of additional oxygen adsorbed

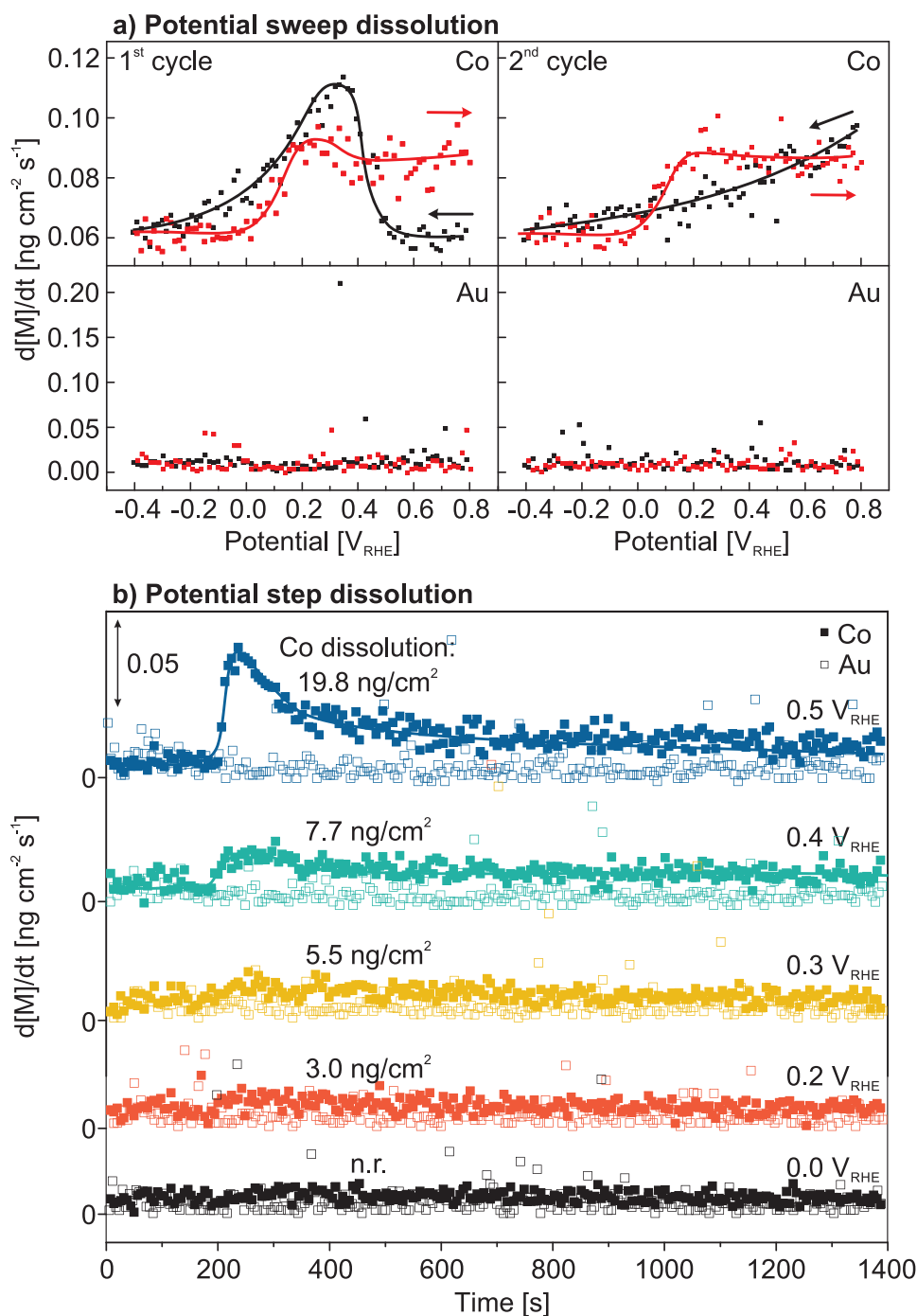


Figure 6. Dissolution of Au and Co measured during a) potential cycling (0.8 to -0.4 V_{RHE}, 2 mV s⁻¹) and b) potential steps from 0.8 V_{RHE} to different potentials (0.5, 0.4, 0.3, 0.2, 0.0 V_{RHE}) at potentials <OCP. The dissolution was measured using EC on-line ICP-MS. Filled squares ■ correspond to ⁵⁹Co, while empty squares □ correspond to ¹⁹⁷Au. For clarity, only 25% of the measured data points are shown in b).

on top of the NIs. The oriented lines are formed to release the strain induced by incorporation of the additional oxygen. Therefore, we assign the appearance of the striped features on the BL islands at 1.2 V_{RHE} to the adsorption and incorporation of additional oxygen from the electrolyte.

For the changes of surface morphology observed at 1.5 V_{RHE}, there are two possible explanations: First, cobalt may be

oxidized from Co³⁺ to Co⁴⁺, which is in principle compatible with the CVs shown in Figure 3b. Oxidation should give rise to restructuring of the islands, and could explain their more corrugated morphology. Second, we may invoke the formation of a gold oxide layer along with the evolution of oxygen at these potentials. Reduction of the oxidized gold surface can lead to formation of small gold islands. In previous ex situ experiments

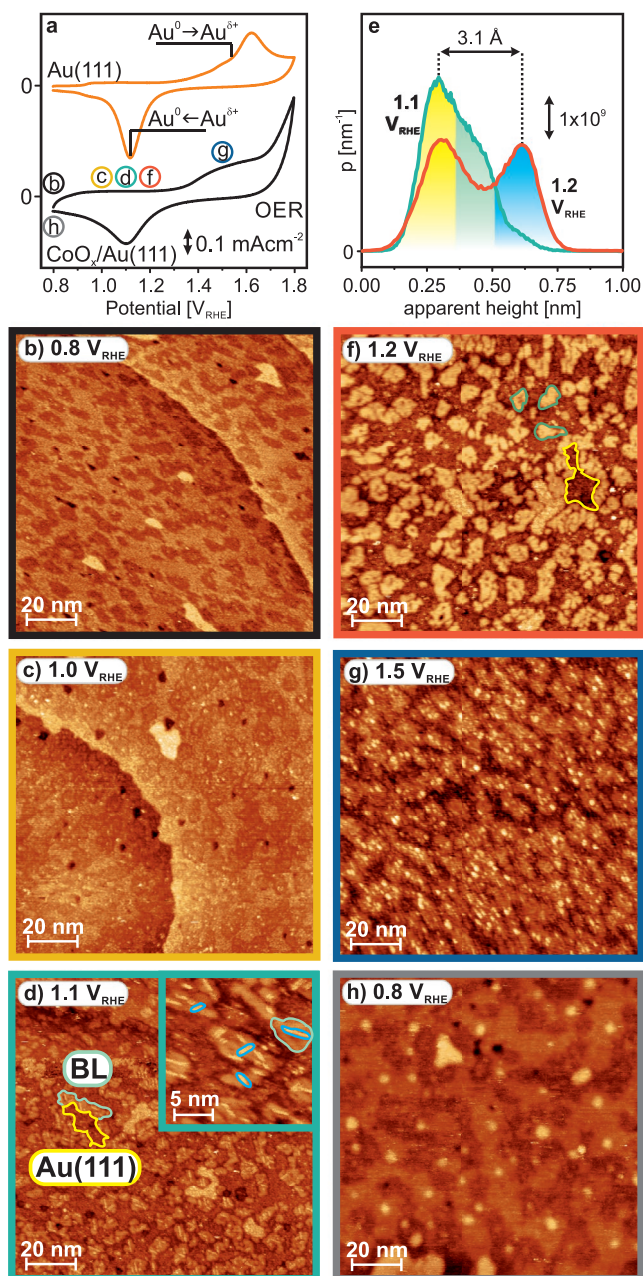


Figure 7. EC-STM images of cobalt oxide NIs supported on Au(111) at potentials above OCP ($0.8 V_{RHE}$). a) Indication of the measuring potentials on the CVs of Au(111) (orange) and $CoO_x/Au(111)$ (black) shown in Figure 3; EC-STM images measured in the anodic scan at b) $0.8 V_{RHE}$, c) $1.0 V_{RHE}$, d) $1.1 V_{RHE}$, f) $1.2 V_{RHE}$, and g) $1.5 V_{RHE}$; h) after keeping a potential of $1.8 V_{RHE}$ for 20 min another STM image was measured at $0.8 V_{RHE}$; e) height distribution determined from (d) and (f). The potential applied to the W-tip was kept constant at $0.35 V_{RHE}$ and the tunneling current was $0.1 nA$.

in $0.1 M NaOH$, some of the authors observed agglomeration of the DL islands after cycling.^[17d] Indeed, comparing the structures observed in Figure 7b,h, we observe a slight increase in the average size of the NI, however, the effect is rather small.

In the next step, we used online ICP-MS to monitor the dissolution of Co and Au at potentials above the OCP

(Figure 8). In analogy to the experiments at low potential, we performed cycling experiments between 0.8 and $1.8 V_{RHE}$ as well as potential step experiments with an initial potential of $0.8 V_{RHE}$ and steps to $1.1, 1.3, 1.5,$ and $1.7 V_{RHE}$, respectively. Each potential step experiment was performed on a new spot of the sample. As a reference, we also performed potential sweep and potential step experiments on bare Au(111) (orange).

We observe that during the potential sweep experiment (Figure 8a), there is minor gold dissolution on both samples upon oxidation of the surface at $1.6 V_{RHE}$. A larger amount of Au is dissolved in the reverse scan at $1.1 V_{RHE}$. The dissolution process is associated with the reduction of the Au oxide layer.^[37] There is almost no difference in the amount of Au dissolved in the first and the second cycle during reduction. In the second cycle, however, Au dissolution is suppressed during oxidation. In the step experiments, (Figure 8b), the amount of dissolved gold increases with increasing potential difference. Noteworthy, we do not detect any cobalt dissolution in both experiments. This finding differs somewhat from the previous ex situ studies in $0.1 M NaOH$.^[17d] In our previous work, we observed that cobalt oxide shows the highest structural stability at pH 10 in phosphate buffer and the stability decreases again with increasing pH.^[29] Therefore we attribute the difference in stability mainly to the effect of the pH and the electrolyte.

Finally we compared the Au dissolution by integration of the ICP-MS signal in the absence and the presence of CoO_x NIs. If the surface is covered by NIs (covering $39\% \pm 6\%$ of a ML), we observe 60% and 20% less Au dissolution in the potential cycling and potential step experiment, respectively. This finding suggests that the cobalt oxide NIs suppress the dissolution of Au underneath the islands.

3. Conclusion

We investigated the structural dynamics, dissolution behavior and electrocatalytic activity of well-defined cobalt oxide NIs supported on Au. The model electrocatalysts were prepared in UHV on Au(111) and characterized and studied in situ in $0.1 M$ phosphate buffer at pH 10. We cover a large potential window ranging from -0.4 up to $1.8 V_{RHE}$ spanning from the HER to the OER range. Specifically, we used CV, EC-STM, and on-line ICP-MS to study changes in structure, morphology, and stability. We summarize the key findings from our work in the following:

Bias Dependent Apparent Height: Cobalt oxide NIs grow on the Au(111) surface as BL and DL structures. Both in STM under ambient conditions and in EC-STM under potential control, we observe an inversion of contrast for the BL islands as a function of the bias voltage. At a bias of $0.4 V$, tunneling through the oxide gives rise to a negative apparent height of the islands with respect to the surface. At a bias voltage of $1.5 V$ tunneling occurs into states of the cobalt oxide giving rise to a positive apparent height. We do not observe any contrast inversion for the DL islands, which we attribute to their smaller band gap. As a result, tunneling always involves states of the DL cobalt oxide itself.

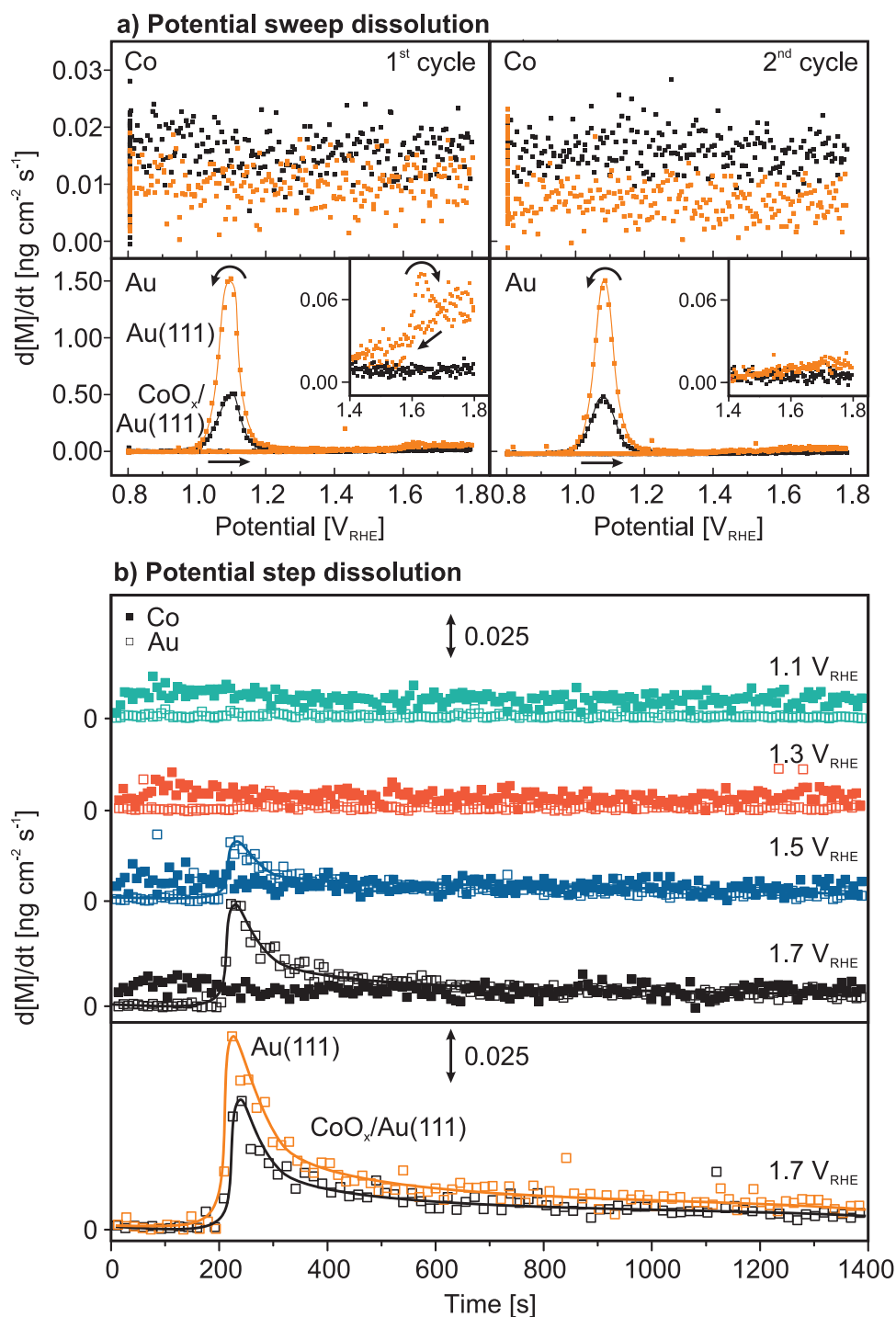


Figure 8. Concentrations of dissolved Au and Co ions measured during a) potential cycling (scan rate $2\ mV\ s^{-1}$) and b) stepwise increase of the potential of cobalt oxide NIs supported on Au(111) above the OCP of $0.8\ V_{RHE}$. The insets show a magnification in the area of 1.4 to $1.9\ V_{RHE}$. The concentrations were measured using EC on-line ICP-MS. Filled squares \blacksquare correspond to ^{59}Co , while empty squares \square correspond to ^{197}Au . For clarity, only 25% of the measured data points are shown in b).

Transfer from UHV and Stability in Electrolyte: By transferring the CoO_x NIs from UHV into the electrolyte the surface of the NIs becomes hydroxylated. Beside this effect, the morphology of the islands remains unchanged upon immersion into electrolyte at the OCP of $0.8\ V_{RHE}$. Additionally we observe no dissolution under these conditions.

Structural Dynamics, Composition, and Dissolution at Potentials Below OCP: Reduction of the cobalt oxide NIs from Co³⁺ to Co²⁺ takes place around $0.4\ V_{RHE}$ and immediately leads to the formation of mobile BL islands. In sharp contrast, the DL islands remain stable under identical conditions. The transition to the dynamic island structure is associated with substantial

dissolution of cobalt, indicating that mobility is associated with the formation of soluble Co^{2+} species in the electrolyte. The dissolution is a transient process that competes with the re-deposition of Co^{2+} species on the electrode surface. We observe the highest dissolution rate when switching the potential from 0.8 to 0.5 V_{RHE} , while the dissolution rate decreases when switching the potentials to lower values. At $-0.3 V_{\text{RHE}}$, metallic cobalt particles are deposited. These structures largely dissolve when returning to more positive potentials and only a small amount of cobalt remains in form of Co^{2+} in BL islands.

Cobalt Oxide Composition, Stability, and Activity at Potentials Above OCP: At 1.0 V_{RHE} , oxygen adatoms adsorb on the surface of the NIs, which initially arrange in form of oriented, striped features, and finally cover the full surface at higher potentials. The Co NIs are highly active toward the OER. No Co dissolution is detectable despite the fact that some agglomeration of the BL NIs is observed. Under OER conditions, the Au(111) support oxidizes and upon subsequent reduction, roughening occurs via deposition of small Au nanoparticles. Noteworthy, the Co NIs are rather stable despite the structural transformation occurring on Au support. Oxidation and reduction of Au is associated with transient dissolution of Au species. The effect is partially suppressed by the cobalt oxide NIs covering the Au(111).

Our findings demonstrate that the morphology and the structural dynamics of cobalt oxide NIs change drastically as a function of the electrode potential. These effects depend critically on both the initial structure of the NIs and the support. The structural transformations are directly correlated with dissolution processes and, therefore, are essential for understanding the stability of the electrocatalytic materials under reaction conditions.

4. Experimental Section

Cleaning of Electrochemical Equipment: All glassware, Teflon equipment, and noble metal wires for CV and EC-STM experiments were stored in a solution of Nochromix (Sigma Aldrich) dissolved in conc. H_2SO_4 (98%_{conc.}, Merck, EMSURE) over night. Prior to the experiments, the equipment was rinsed five times with ultrapure water (MilliQ synergy UV, 18.2 $\text{M}\Omega\text{cm}$ at 25 °C, < 5 ppb total organic carbon) and subsequently boiled three times in ultrapure water. 0.1 M phosphate buffer at pH 10 was used as supporting electrolyte, which was prepared using ultrapure water, Na_2HPO_4 (Merck, Suprapur, 99.99 %), and NaOH (Sigma Aldrich, 99.99 %).

UHV Sample Preparation: To prepare the cobalt oxide NIs for the measurements at ambient pressures (CV, STM, EC-STM, and online ICP-MS), a UHV system located at the Friedrich-Alexander-Universität Erlangen-Nürnberg, was used which consists of a preparation chamber with a base pressure of 2×10^{-10} mbar and a dedicated transfer system. For a detailed description of the setup, we refer to literature.^[38] The cobalt oxide NIs were prepared in UHV on an Au(111) single crystal (MaTeck, 99.999%, $d = 10$ mm, roughness < 10 nm, accuracy < 0.1°) following a procedure described previously.^[17a] The crystal was cleaned by multiple cycles of Ar^+ bombardment (Linde 6.0, 8×10^{-5} mbar, 1.2 keV, 300 K) and subsequent annealing in UHV at 773 K for 30 min. Cobalt (Alfa Aesar, 99.95 %, 2 mm rod) was deposited by physical vapor deposition in O_2 (1×10^{-6} mbar) at a sample temperature of 378 K. Prior to the experiments, the deposition rate was calibrated by means of a quartz microbalance and the evaporation time was adjusted to give a nominal Co coverage of 1/3 of a ML (1 ML defined as the number density of Au(111) surface atoms). Afterward, the crystal was post-annealed at 523 K in O_2 (1×10^{-6} mbar) for 10 min, followed by annealing in UHV

for 5 min. After preparation, the sample was transferred from UHV to ambient conditions and immediately mounted in the EC cells.

CV: The EC characterization of the samples was performed by CV. A Pt wire (MaTeck, 99.9%) served as a counter electrode (CE) and a commercial Ag/AgCl (ALS, 3 M NaCl, 0.195 V_{NHE}) electrode as reference electrode (RE). To avoid chloride contaminations, the compartment of the RE was separated from the measuring cell via a stop cock. Note that all potentials in this work are referred to the reversible hydrogen electrode (RHE). 0.1 M phosphate buffer solution at pH 10 was used as electrolyte. The sample was immersed into the degassed electrolyte (N_2 , Linde 5.0, 30 min) in hanging meniscus configuration (see Figure 1) at a potential of 0.8 V_{RHE} . The voltammograms were recorded with a scan rate of 0.05 V s^{-1} . Potential control was established by means of a commercial potentiostat (Gamry, Reference 600+).

UHV STM: The UHV STM experiments were carried out in a UHV chamber with a base pressure better than 2×10^{-10} mbar located at the University of Aarhus. A Au(111) single crystal (MaTeck, 99.999%, roughness < 10 nm, accuracy < 0.1°) was used as the support and it was cleaned by repeated cycles of Ar^+ sputtering (Linde, 6.0, 2×10^{-7} mbar, 1.5 keV at room temperature, 30 min) and annealing (800 K, 15 min). For the CoO_x NIs, the preparation procedure as described above was followed. For deposition, an electron-beam evaporator (Mantis Deposition Ltd, QUAD-EV-C mini e-beam evaporator) equipped with a cobalt rod (Goodfellow Cambridge Ltd., 99.99+%, 2 mm diameter) was used. The resulting islands were imaged using an “Aarhus-type” STM. All the STM images were acquired at room temperature (≈ 297 K).

EC-STM: The EC-STM and STM experiments at ambient pressure were performed with a Keysight Technologies system (Series 5500 AFM/SPM) equipped with a bipotentiostat, which controls the tip potential and the sample potential independently. The STM is isolated from electric, mechanic, and acoustic vibrations by a combination of active and passive noise damping. STM images in air were acquired using mechanically cut PtIr tips (80:20, 99.9%, MaTeck). For the EC-STM experiments, a home-built Teflon cell was used with an electrolyte volume of 0.8 mL. The Teflon cell was pressed against the sample via an O-Ring (Kalrez) for sealing. Similar as in the CV experiments, a Pt wire (MaTeck, 99.9%) was used as CE and a miniature Ag/AgCl (DriRef-2SH, World Precision Instruments 3 M KCl, 0.195 V_{NHE}) as RE. In the EC-STM experiments, electrochemically etched PtIr (80:20, 99.9%, MaTeck) and W (99.95%, Alfa Aesar) tips were used, which were coated with Apiezon wax (Apiezon Wax W, Apiezon). The PtIr tips were etched electrochemically following a procedure adapted by Friebel et al.^[39] The PtIr wire was passed through a Pt (MaTeck, 99.9%) ring with a diameter of 1.5 cm used as CE and immersed in a solution of 2 M KOH and 4 M KSCN. The immersed part of the wire was isolated from the solution by a Teflon tube. Only a small part of the wire (above the Teflon tube) was in contact with the solution. For etching, a rectangular etching voltage (1 kHz, $V_{\text{pp}} = 10$ V, $V_{\text{DC}} = 2$ V) was applied until the lower part of the wire dropped off. Electrochemically etched W tips were produced by applying a voltage of 2 V to a W wire, which was passed through a Pt (MaTeck, 99.9%) ring CE ($d = 5$ mm). The ring electrode held a lamella of 2 M KOH (85%, Merck).

As STM tips, the lower parts of the PtIr and W wires were used. After etching, the tips were cleaned in ultrapure water and coated with molten Apiezon wax. This treatment reduces the Faradaic currents on the tip in the tip potential region of interest below 10 pA. Before and during the EC-STM measurement, the EC-STM cell was placed in an environmental chamber purged with N_2 (5.0, Linde). At the beginning of the EC-STM measurements, images were obtained at a sample potential of 0.8 V_{RHE} and tip potentials with minor faradaic currents (0.3–0.4 V_{RHE} for W, 0.4 V–0.5 V_{RHE} for PtIr) were used. Afterward, the potential applied to the sample was varied, while the tip potential was kept constant. The tunneling parameters of the acquired images are given in the respective figure captions. STM images were post-processed (row-aligning, data leveling) using the Gwyddion software (version 2.55).^[40]

EC On-Line ICP-MS: EC on-line ICP-MS measurements were performed using a home-build three-electrode SFC coupled to an inductively coupled plasma mass spectrometer (ICP-MS, Perkin Elmer, NexION 350X). To contact the sample the SFC had an opening with a

diameter of 1 mm and a silicon sealing. A graphite rod (Sigma Aldrich, 99.995% trace metal basis) served as CE mounted at the inlet, while an Ag/AgCl electrode (Metrohm, 3 m KCl, 0.195 V_{NHE}) served as RE closely connected via a 0.4 mm capillary to the working electrode surface. For a more detailed description of the setup, we refer to literature.^[41] The flow rate of the cell was $\approx 3.6 \mu\text{L s}^{-1}$. A time delay of 20 s between dissolution at the sample and detection at the ICP-MS was subtracted to directly correlate the applied potential and dissolution data. ⁵⁹Co and ¹⁹⁷Au were recorded in parallel with a dwell time of 50 μs each, using ⁷⁴Ge and ¹⁸⁷Re as internal standards. The measurements were performed with a 0.05 m solution of Na₂HPO₄ at pH 10. During the experiment, the electrolyte was purged with Ar (5.0, Air Liquide). The small diameter of the opening enabled to measure multiple spots on the same sample. Each measurement spot was contacted at a potential of 0.8 V_{RHE}. Afterward, a CV (2 mV s⁻¹) or a potential step was applied to the sample. The ICP-MS was calibrated prior to the experiments with solutions of 0, 0.5, 1, and 5 $\mu\text{g L}^{-1}$ of the measured metals.

Supporting Information

Supporting Information is available from the Wiley Online Library or from the author.

Acknowledgements

The authors acknowledge financial support by the Deutsche Forschungsgemeinschaft (DFG) (project 431733372) and additional support by the DFG (Research Unit FOR 1878 “Functional Molecular Structures on Complex Oxide Surfaces”, projects 214951840, 322419553, CH 1763/5-1). The authors acknowledge financial support by the German Federal Ministry of Education and Research (BMBF, Project Combined Infrared and X-Ray Analytics of Energy Materials, CIXenergy 05K19WE1) and by the Bavarian Ministry of Economic Affairs, Regional Development and Energy. Further, this work was supported by the European Union’s Horizon 2020 research and innovation programme under grant agreement CREATE [721065]. The authors are grateful to Ulrike Diebold and Stijn Mertens for great support. C.S. and O.B. are particularly thankful for hosting their research visits. J.V.L, J.R.F and Z.S acknowledge Carlsbergfondet (Project CF18-0071) and Villumfonden (Project 13264).

Open access funding enabled and organized by Projekt DEAL.

Conflict of Interest

The authors declare no conflict of interest.

Keywords

cobalt oxide, electrocatalysis, electrochemical scanning tunneling microscopy, model catalysis, oxygen evolution reaction

Received: November 18, 2020

Revised: December 9, 2020

Published online: January 18, 2021

- [1] a) Y. Jiao, Y. Zheng, M. Jaroniec, S. Z. Qiao, *Chem. Soc. Rev.* **2015**, *44*, 2060; b) I. Roger, M. A. Shipman, M. D. Symes, *Nat. Rev. Chem.* **2017**, *1*, 0003; c) J. Wang, W. Cui, Q. Liu, Z. Xing, A. M. Asiri, X. Sun, *Adv. Mater.* **2016**, *28*, 215; d) N.-T. Suen, S.-F. Hung, Q. Quan, N. Zhang, Y.-J. Xu, H. M. Chen, *Chem. Soc. Rev.* **2017**, *46*, 337.
- [2] J. Wang, W. Cui, Q. Liu, Z. Xing, A. M. Asiri, X. Sun, *Adv. Mater.* **2016**, *28*, 215.
- [3] S. Trasatti, *Electrochim. Acta* **1984**, *29*, 1503.
- [4] a) I. C. Man, H.-Y. Su, F. Calle-Vallejo, H. A. Hansen, J. I. Martínez, N. G. Inoglu, J. Kitchin, T. F. Jaramillo, J. K. Nørskov, J. Rossmeisl, *ChemCatChem* **2011**, *3*, 1159; b) N. B. Halck, V. Petrykin, P. Krtil, J. Rossmeisl, *Phys. Chem. Chem. Phys.* **2014**, *16*, 13682; c) M. Bajdich, M. García-Mota, A. Vojvodic, J. K. Nørskov, A. T. Bell, *J. Am. Chem. Soc.* **2013**, *135*, 13521; d) M. Zhang, M. de Respinis, H. Frei, *Nat. Chem.* **2014**, *6*, 362; e) R. Subbaraman, D. Tripkovic, K.-C. Chang, D. Strmcnik, A. P. Paulikas, P. Hirunsit, M. Chan, J. Greeley, V. Stamenkovic, N. M. Markovic, *Nat. Mater.* **2012**, *11*, 550; f) L. Liao, Q. Zhang, Z. Su, Z. Zhao, Y. Wang, Y. Li, X. Lu, D. Wei, G. Feng, Q. Yu, X. Cai, J. Zhao, Z. Ren, H. Fang, F. Robles-Hernandez, S. Baldelli, J. Bao, *Nat. Nanotechnol.* **2014**, *9*, 69; g) J. Suntivich, K. J. May, H. A. Gasteiger, J. B. Goodenough, Y. Shao-Horn, *Science* **2011**, *334*, 1383; h) N. H. Chou, P. N. Ross, A. T. Bell, T. D. Tilley, *ChemSusChem* **2011**, *4*, 1566; i) B. Zhang, X. Zheng, O. Voznyy, R. Comin, M. Bajdich, M. García-Melchor, L. Han, J. Xu, M. Liu, L. Zheng, F. P. García de Arquer, C. T. Dinh, F. Fan, G. Yuan, E. Yassitepe, N. Chen, T. Regier, P. Liu, Y. Li, P. De Luna, A. Janmohamed, H. L. Xin, H. Yang, A. Vojvodic, E. H. Sargent, *Science* **2016**, *352*, 333; j) H. Bode, K. Dehmelt, J. Witte, *Electrochim. Acta* **1966**, *11*, 1079.
- [5] a) L. Trotochaud, J. K. Ranney, K. N. Williams, S. W. Boettcher, *J. Am. Chem. Soc.* **2012**, *134*, 17253; b) J. Yang, K. Walczak, E. Anzenberg, F. M. Toma, G. Yuan, J. Beeman, A. Schwartzberg, Y. Lin, M. Hettick, A. Javey, J. Yano, H. Frei, I. D. Sharp, *J. Am. Chem. Soc.* **2014**, *136*, 6191; c) J. B. Gerken, J. G. McAlpin, J. Y. C. Chen, M. L. Rigsby, W. H. Casey, R. D. Britt, S. S. Stahl, *J. Am. Chem. Soc.* **2011**, *133*, 14431.
- [6] a) M. Pourbaix, *Atlas of Electrochemical Equilibria in Aqueous Solutions*, NACE, Houston **1974**; b) A. Foelske, H.-H. Strehblow, *Surf. Interface Anal.* **2002**, *34*, 125; c) J. G. McAlpin, Y. Surendranath, M. Dincă, T. A. Stich, S. A. Stoian, W. H. Casey, D. G. Nocera, R. D. Britt, *J. Am. Chem. Soc.* **2010**, *132*, 6882.
- [7] a) D. Friebe, M. Bajdich, B. S. Yeo, M. W. Louie, D. J. Miller, H. Sanchez Casalongue, F. Mbuga, T.-C. Weng, D. Nordlund, D. Sokaras, R. Alonso-Mori, A. T. Bell, A. Nilsson, *Phys. Chem. Chem. Phys.* **2013**, *15*, 17460; b) J. Yang, J. K. Cooper, F. M. Toma, K. A. Walczak, M. Favaro, J. W. Beeman, L. H. Hess, C. Wang, C. Zhu, S. Gul, J. Yano, C. Kisielowski, A. Schwartzberg, I. D. Sharp, *Nat. Mater.* **2017**, *16*, 335.
- [8] B. S. Yeo, A. T. Bell, *J. Am. Chem. Soc.* **2011**, *133*, 5587.
- [9] a) M. Favaro, J. Yang, S. Nappini, E. Magnano, F. M. Toma, E. J. Crumlin, J. Yano, I. D. Sharp, *J. Am. Chem. Soc.* **2017**, *139*, 8960; b) E. Fabbri, M. Nachtegaal, T. Binninger, X. Cheng, B.-J. Kim, J. Durst, F. Bozza, T. Graule, R. Schaublin, L. Wiles, M. Pertoso, N. Danilovic, K. E. Ayers, T. J. Schmidt, *Nat. Mater.* **2017**, *16*, 925.
- [10] a) A. M. Ullman, C. N. Brodsky, N. Li, S.-L. Zheng, D. G. Nocera, *J. Am. Chem. Soc.* **2016**, *138*, 4229; b) T. Ling, D.-Y. Yan, Y. Jiao, H. Wang, Y. Zheng, X. Zheng, J. Mao, X.-W. Du, Z. Hu, M. Jaroniec, S.-Z. Qiao, *Nat. Commun.* **2016**, *7*, 12876.
- [11] a) F. Jiao, H. Frei, *Energy Environ. Sci.* **2010**, *3*, 1018; b) M. Grzelczak, J. Zhang, J. Pfrommer, J. Hartmann, M. Driess, M. Antonietti, X. Wang, *ACS Catal.* **2013**, *3*, 383; c) J. Rosen, G. S. Hutchings, F. Jiao, *J. Am. Chem. Soc.* **2013**, *135*, 4516; d) F. Cheng, J. Shen, B. Peng, Y. Pan, Z. Tao, J. Chen, *Nat. Chem.* **2011**, *3*, 79; e) F. Song, X. Hu, *J. Am. Chem. Soc.* **2014**, *136*, 16481; f) F. Song, X. Hu, *Nat. Commun.* **2014**, *5*, 4477.
- [12] a) K. Fominykh, P. Chernev, I. Zaharieva, J. Sicklinger, G. Stefanic, M. Döblinger, A. Müller, A. Pokharel, S. Böcklein, C. Scheu, T. Bein, D. Fattakhova-Rohlfing, *ACS Nano* **2015**, *9*, 5180; b) Z. Wang, H. Liu, R. Ge, X. Ren, J. Ren, D. Yang, L. Zhang, X. Sun, *ACS Catal.* **2018**, *8*, 2236.
- [13] a) L. C. Seitz, T. J. P. Hersbach, D. Nordlund, T. F. Jaramillo, *J. Phys. Chem. Lett.* **2015**, *6*, 4178; b) X. Lu, Y. H. Ng, C. Zhao, *ChemSusChem* **2014**, *7*, 82.

- [14] a) D. A. H. Cunningham, T. Kobayashi, N. Kamijo, M. Haruta, *Catal. Lett.* **1994**, 25, 257; b) Y. Liu, H. Dai, J. Deng, S. Xie, H. Yang, W. Tan, W. Han, Y. Jiang, G. Guo, *J. Catal.* **2014**, 309, 408; c) S. Back, M. H. Hansen, J. A. Garrido Torres, Z. Zhao, J. K. Nørskov, S. Siahrostami, M. Bajdich, *ACS Appl. Mater. Interfaces* **2019**, 11, 2006; d) B. Y. Kim, I.-B. Shim, Z. O. Araci, S. S. Saavedra, O. L. A. Monti, N. R. Armstrong, R. Sahoo, D. N. Srivastava, J. Pyun, *J. Am. Chem. Soc.* **2010**, 132, 3234; e) R. Frydendal, M. Busch, N. B. Halck, E. A. Paoli, P. Krtil, I. Chorkendorff, J. Rossmeisl, *ChemCatChem* **2015**, 7, 149; f) A. L. Strickler, M. a. Escudero-Escribano, T. F. Jaramillo, *Nano Lett.* **2017**, 17, 6040.
- [15] D. M. Kolb, *Angew. Chem., Int. Ed.* **2001**, 40, 1162.
- [16] a) F. Faisal, C. Stumm, M. Bertram, F. Waidhas, Y. Lykhach, S. Cherevko, F. Xiang, M. Ammon, M. Vorokhta, B. Šmíd, T. Skála, N. Tsud, A. Neitzel, K. Beranová, K. C. Prince, S. Geiger, O. Kasian, T. Wähler, R. Schuster, M. A. Schneider, V. Matolín, K. J. J. Mayrhofer, O. Brummel, J. Libuda, *Nat. Mater.* **2018**, 17, 592; b) O. Brummel, J. Libuda, *Catal. Lett.* **2020**, 150, 1546; c) F. Buchner, M. Eckardt, T. Böhler, J. Kim, J. Gerlach, J. Schnaidt, R. J. Behm, *ChemSusChem* **2020**, 13, 3199; d) M. Bertram, C. Prössl, M. Ronovský, J. Knöppel, P. Matvija, L. Fusek, T. Skála, N. Tsud, M. Kastenmeier, V. Matolín, K. J. J. Mayrhofer, V. Johánek, J. Mysliveček, S. Cherevko, Y. Lykhach, O. Brummel, J. Libuda, *J. Phys. Chem. Lett.* **2020**, 11, 8365.
- [17] a) A. S. Walton, J. Fester, M. Bajdich, M. A. Arman, J. Osiecki, J. Knudsen, A. Vojvodic, J. V. Lauritsen, *ACS Nano* **2015**, 9, 2445; b) J. Fester, M. Bajdich, A. S. Walton, Z. Sun, P. N. Plessow, A. Vojvodic, J. V. Lauritsen, *Top. Catal.* **2017**, 60, 503; c) J. Fester, M. García-Melchor, A. S. Walton, M. Bajdich, Z. Li, L. Lammich, A. Vojvodic, J. V. Lauritsen, *Nat. Commun.* **2017**, 8, 14169; d) J. Fester, A. Makoveev, D. Grumelli, R. Gutzler, Z. Sun, J. Rodríguez-Fernández, K. Kern, J. V. Lauritsen, *Angew. Chem., Int. Ed.* **2018**, 57, 11893; e) J. Fester, Z. Sun, J. Rodríguez-Fernández, A. Walton, J. V. Lauritsen, *J. Phys. Chem. B* **2018**, 122, 561; f) J. Fester, Z. Sun, J. Rodríguez-Fernández, A. S. Walton, J. V. Lauritsen, *J. Phys. Chem. C* **2019**, 123, 9176; g) J. Fester, A. Walton, Z. Li, J. V. Lauritsen, *Phys. Chem. Chem. Phys.* **2017**, 19, 2425.
- [18] a) N. Hodnik, G. Dehm, K. J. J. Mayrhofer, *Acc. Chem. Res.* **2016**, 49, 2015; b) A. A. Gewirth, B. K. Niece, *Chem. Rev.* **1997**, 97, 1129; c) K. Itaya, *Prog. Surf. Sci.* **1998**, 58, 121.
- [19] a) G. Serrano, B. Bonanni, M. Di Giovannantonio, T. Kosmala, M. Schmid, U. Diebold, A. Di Carlo, J. Cheng, J. VandeVondele, K. Wandelt, C. Goletti, *Adv. Mater. Interfaces* **2015**, 2, 1500246; b) M. Müllner, J. Balajka, M. Schmid, U. Diebold, S. F. L. Mertens, *J. Phys. Chem. C* **2017**, 121, 19743.
- [20] F. Ringleb, Y. Fujimori, H.-F. Wang, H. Ariga, E. Carrasco, M. Sterrer, H.-J. Freund, L. Giordano, G. Pacchioni, J. Goniakowski, *J. Phys. Chem. C* **2011**, 115, 19328.
- [21] S. Ando, T. Suzuki, K. Itaya, *J. Electroanal. Chem.* **1997**, 431, 277.
- [22] A. Foelske, J. Kunze, H.-H. Strehblow, *Surf. Sci.* **2004**, 554, 10.
- [23] C. Wöll, S. Chiang, R. J. Wilson, P. H. Lippel, *Phys. Rev. B* **1989**, 39, 7988.
- [24] I. Sebastian, T. Bertrams, K. Meinel, H. Neddermeyer, *Faraday Discuss.* **1999**, 114, 129.
- [25] I. Sebastian, H. Neddermeyer, *Surf. Sci.* **2000**, 454–456, 771.
- [26] M. Santis, A. Buchsbaum, P. Varga, M. Schmid, *Phys. Rev. B* **2011**, 84, 125430.
- [27] A. Picone, M. Riva, A. Brambilla, D. Giannotti, O. Ivashko, G. Bussetti, M. Finazzi, F. Ciccacci, L. Duò, *J. Phys. Chem. C* **2016**, 120, 5233.
- [28] Y. Lykhach, S. Piccinin, T. Skála, M. Bertram, N. Tsud, O. Brummel, M. Farnesi Camellone, K. Beranová, A. Neitzel, S. Fabris, K. C. Prince, V. Matolín, J. Libuda, *J. Phys. Chem. Lett.* **2019**, 10, 6129.
- [29] F. Faisal, M. Bertram, C. Stumm, S. Cherevko, S. Geiger, O. Kasian, Y. Lykhach, O. Lytken, K. J. J. Mayrhofer, O. Brummel, J. Libuda, *J. Phys. Chem. C* **2018**, 122, 7236.
- [30] J. Chivot, L. Mendoza, C. Mansour, T. Pauporté, M. Cassir, *Corros. Sci.* **2008**, 50, 62.
- [31] P. Rodriguez, J. M. Feliu, M. T. M. Koper, *Electrochem. Commun.* **2009**, 11, 1105.
- [32] R. L. Doyle, I. J. Godwin, M. P. Brandon, M. E. G. Lyons, *Phys. Chem. Chem. Phys.* **2013**, 15, 13737.
- [33] C. Schlaup, S. Horch, *Surf. Sci.* **2013**, 608, 44.
- [34] K. Morgenstern, J. Kibsgaard, J. V. Lauritsen, E. Lægsgaard, F. Besenbacher, *Surf. Sci.* **2007**, 601, 1967.
- [35] a) M. Kleinert, H. F. Waibel, G. E. Engelmann, H. Martin, D. M. Kolb, *Electrochim. Acta* **2001**, 46, 3129; b) N. Di, A. Damian, F. Maroun, P. Allongue, *J. Electrochem. Soc.* **2016**, 163, D3062.
- [36] H. Zeuthen, W. Kudernatsch, G. Peng, L. R. Merte, L. K. Ono, L. Lammich, Y. Bai, L. C. Grabow, M. Mavrikakis, S. Wendt, F. Besenbacher, *J. Phys. Chem. C* **2013**, 117, 15155.
- [37] a) S. Cherevko, A. R. Zeradjanin, G. P. Keeley, K. J. J. Mayrhofer, *J. Electrochem. Soc.* **2014**, 161, H822; b) M. Schalenbach, O. Kasian, M. Ledendecker, F. D. Speck, A. M. Mingers, K. J. J. Mayrhofer, S. Cherevko, *Electrocatalysis* **2018**, 9, 153.
- [38] F. Faisal, M. Bertram, C. Stumm, F. Waidhas, O. Brummel, J. Libuda, *Rev. Sci. Instrum.* **2018**, 89, 114101.
- [39] D. Friebe, C. Schlaup, P. Broekmann, K. Wandelt, *Surf. Sci.* **2006**, 600, 2800.
- [40] D. Nečas, P. Klapetek, *Cent. Eur. J. Phys.* **2012**, 10, 181.
- [41] S. O. Klemm, A. A. Topalov, C. A. Laska, K. J. J. Mayrhofer, *Electrochem. Commun.* **2011**, 13, 1533.